



## Three-dimensional kinematics of the India–Eurasia collision

Lifeng Wang <sup>1,2,3</sup>✉ & Sylvain Barbot <sup>4</sup>✉

The collision between India and Eurasia mobilizes multiple processes of continental tectonics. However, how deformation develops within the lithosphere across the Tibetan Plateau is still poorly known and a synoptic view is missing. Here, we exploit an extensive geodetic observatory to resolve the kinematics of this diffuse plate boundary and the arrangement of various mechanisms down to upper-mantle depths. The three-dimensional velocity field is compatible with continental underthrusting below the central Himalayas and with delamination rollback below the western syntaxis. The rise of the Tibetan Plateau occurs by shortening in the Indian and Asian crusts at its southern and northwestern margins. The subsidence of Central Tibet is associated with lateral extrusion and attendant lithospheric thinning aided by the downwelling current from the opposite-facing Indian and Asian collisions. The current kinematics of the Indian–Eurasian collision may reflect the differential evolution of the inner and outer Tibetan Plateau during the late Cenozoic.

<sup>1</sup>State Key Laboratory of Earthquake Dynamics, Institute of Geology, China Earthquake Administration, Huayanli Jia 1, Chaoyang, Beijing 100029, China.

<sup>2</sup>Lhasa National Geophysical Observation and Research Station, Beijing, China. <sup>3</sup>Xinjiang Pamir Intracontinental Subduction National Observation and Research Station, Beijing, China. <sup>4</sup>Department of Earth Sciences, University of Southern California, 3651 Trousdale Pkwy, Los Angeles, CA 90089, USA.

✉email: [wanglf@ies.ac.cn](mailto:wanglf@ies.ac.cn); [sbarbot@usc.edu](mailto:sbarbot@usc.edu)

The diffuse collision between the Indian and Eurasian plates sheds light on the processes of continental tectonics, which are more complex than in the oceanic parts of the Earth. The rise of the Tibetan Plateau may have occurred by continental underthrusting<sup>1–3</sup>, but the limited extent of the Great Indian slab, terminating south of the Banggong-Nujiang Suture (BNS)<sup>4–6</sup>, requires one or more episodes of slab break-off and foundering<sup>7</sup> or delamination rollback of the Indian lithosphere allowing injection of a thin sliver of Indian crust<sup>8–11</sup>. Across the region, the retreat and rollback of Asian subduction may have contributed to the growth of the Tibetan Plateau from the north<sup>12,13</sup>. Inside the plateau, east-west extrusion is partitioned along the longitudinal Karakoram Fault (KRF), Altyn Tagh Fault (ATF), Xiansuihe-Xiaojiang Fault (XXF), Kunlun Fault (KLF), and Haiyuan Fault (HYF) strike-slip faults and the latitudinal rift zones<sup>13–15</sup>. The east-west extrusion of the Tibetan crust<sup>16,17</sup> and the outward motion of the Yunnan province and the Shan Plateau<sup>18</sup> demonstrate the influence of far-field boundary conditions<sup>19,20</sup>, particularly slab rollback in the Western Pacific and Sunda subduction zones<sup>21,22</sup> and rigid motion of the Tarim and Sichuan basins<sup>23</sup>. Geological observations<sup>7,9,24–34</sup> and geodynamic models of the lithosphere<sup>35–41</sup> have brought great insights into the timing and growth mechanisms of the Tibetan Plateau. Yet, the internal deformation of the lithosphere within the diffuse plate boundary and the arrangement of the tectonic structures remain elusive<sup>42</sup>. Additional constraints on the tectonic processes that shape the Tibetan Plateau can be derived from present-day geodetic measurements (Fig. 1), as the surface deformation is a direct measure of the material response to the internal forces and boundary conditions<sup>43–46</sup>. These observations have been interpreted in terms of rotating elastic blocks bounded by faults<sup>47–51</sup> or as the result of interseismic locking of plate-boundary type faults<sup>52–54</sup>. However, these models assume restrictive rheology for the continental crust that forbids distributed deformation, and the architecture of the lower crust and upper mantle of the Tibetan Plateau is often simplified to vertical faults.

Here, we present a three-dimensional kinematic model of the Indian-Eurasian collision based on a recently developed method<sup>55–58</sup> to provide new constraints on the mechanisms deforming the Tibetan Plateau and to illuminate the spatial arrangement of the processes involved. The model encompasses localized deformation by fault creep in the upper crust and mid-crust as well as distributed deformation in the lower crust and upper mantle to provide a consistent image of the internal deformation of the continental lithosphere. In the following sections, we describe the geodetic observations, explain how we construct and calibrate the kinematic model, and discuss the implications for continental tectonics around the Indian-Eurasian collision. The model captures the trajectory of the Indian slab as it descends below the Himalayan Arc and the progression of the Asian slab as it collides with the northern Tibetan Plateau and subducts underneath the Pamir, and offers some constraints on the forces that operate within the intervening diffuse plate boundary. The inferred style of Indian subduction varies with longitude and depth, with frontal collision against the Asian lithosphere underneath the Hindu-Kush, delamination rollback of the Indian lithosphere near the west and east Himalayan syntaxes, and low-angle underthrusting beneath the central and eastern Himalayas. The tectonic stress regime varies gradually from compression, to shear, and to extension from the edge of the Tibetan Plateau to Central Tibet, compatible with the dominant type of seismicity. The change of stress orientation accompanies different patterns of vertical displacement: While the margins of the Tibetan Plateau are growing, Central Tibet is subsiding relative to Inner Mongolia.

## Results

**Geodetic observations and modeling assumptions.** The present-day tectonic deformation accommodating the Indian-Eurasian collision is recorded by an extensive geodetic observatory (Fig. 1) that blankets the Tibetan Plateau from India to Eurasia and from the Pamir-Tien shan ranges to the Sichuan Basin<sup>17,54,59–63</sup>. We consider a geodetic velocity field consisting of 2870 horizontal and 450 vertical velocity vectors that capture the secular deformation of the entire collision zone (Fig. 1). The horizontal velocity field is presented in a local reference frame free of overall

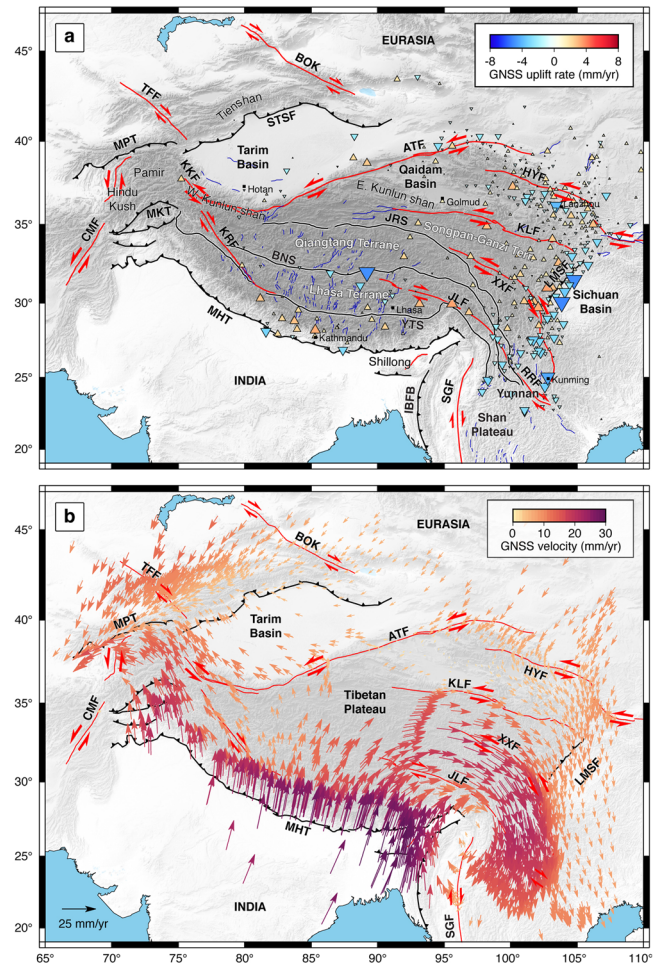


**Fig. 1** Tectonic context and GNSS velocity field around the Tibetan Plateau. **a** Tectonic terranes, sutures<sup>82</sup>: BNS Banggong-Nujiang Suture, JRS Jinsha Suture, YTS Yarlung Tsangpo Suture, and faults<sup>13,61,82,133</sup>: ATF Altyn Tagh Fault, BOK Boluokenu Fault, CMF Chaman Fault, HYF Haiyuan Fault, IBFB Indo-Burman Fold and Thrust belt, JLF Jiali Fault, KKF Karakax fault, KLF Kunlun Fault, KRF Karakoram Fault, LMSF Longmen shan Fault, MHT Main Himalayan Thrust, MKT Main Karakorum Thrust, MPT Main Pamir Thrust, RRF Red River Fault, STSF South Tien shan Fault, SGF Sagaing Fault, TFF Talas-Fergana Fault, XXF Xiansuihe-Xiaojiang Fault. The vertical velocity field (colored triangles pointing up and down for uplift and subsidence, respectively) is relative to site far north of the Tibetan Plateau<sup>63</sup>. In this reference frame, subsidence takes place in Central Tibet, the Tarim basin, and in the Yunnan Province and Shan Plateau. **b** Horizontal velocity field in a reference frame without net rotation or translation that can be decomposed into rotations about three Euler poles (Fig. S1) showing the convergence of India and Eurasia towards the Tibetan Plateau and tectonic escape about the western and eastern syntaxes, apparently through—not around—the Tarim and Sichuan basins.

translation and rotation of the GPS observations (Fig. S1), highlighting the latitudinal shortening and the east-west extension pivoting in Central Tibet. The vertical velocity field is expressed relative to distant sites northeast of the Tibetan Plateau in Inner Mongolia<sup>63</sup>, revealing ongoing subsidence of Central Tibet, the Tarim and Sichuan basins, and the Yunnan province. We interpret the relative subsidence of Central Tibet to be of tectonic origin because the melting of high-altitude glaciers only causes a small rebound in the other direction<sup>64</sup>. Therefore, the vertical velocity field provides additional constraints on the internal deformation of the Tibetan Plateau.

We construct a three-dimensional kinematic model of tectonic deformation across the collision zone exploiting the elastic coupling between deep-seated plastic deformation and the surrounding lithosphere that operates at short time scales. Whether the Tibetan crust and mantle are coupled or decoupled over geological time scales remains debated. A weak lower crust may decouple the continental crust from the underlying mantle over time scales much longer than the seismic cycle<sup>18,65</sup>. However, seismological and geodetic studies<sup>66–71</sup> and geodynamic simulations<sup>37,41,72</sup> suggest coherent crustal and mantle deformation. Regardless of the behavior at geological time scales, elastic coupling still operates at time scales shorter than the characteristic relaxation time of the Tibetan lower crust, which is of the order of a hundred years<sup>37</sup>. As such, geodetic measurements of postseismic and seasonal deformation have been widely used to understand lower-crustal and upper mantle rheology<sup>56,73–81</sup>. Likewise, we constrain deep-seated plastic deformation without time dependency using the interseismic velocity field.

The structural model combines surface and volume elements (Fig. S2) that represent localized faulting in the brittle crust and distributed deformation in the deep plastic substrate, respectively. The surface elements of faults are built from geological and seismological observations<sup>13,53,82,83</sup> and the volume elements follow the Moho<sup>84</sup>, sampled horizontally every 70 km. The volume elements capture the deep deformation that occurs by faulting, localized shear zones, or other types of thermodynamically irreversible processes. The observed velocity field can be modeled as a linear combination of slip velocity and plastic strain rate within surface and volume elements, respectively (Figs. S3 and S4).

One of the major unknowns about the mechanics of the diffuse Indian-Eurasian collision zone is the depths where plastic deformation accumulates. Latitudinal shortening can be accommodated primarily by mantle flow, as is typical in a subduction setting. Alternatively, plastic deformation may concentrate in the weak lower crust, as indicated by the dearth of earthquakes at these depths and typical strength profiles of the continental lithosphere based on quartz, wet feldspar, or a granulite rheology<sup>85,86</sup>. Another debate concerns the depth extent of continental strike-slip faults, i.e., whether they only occupy the brittle crust or extend much deeper into the upper mantle as localized shear zones<sup>47,87</sup>. To explore these hypotheses, we test three different end-member lithospheric models. In all cases, we use the same fault geometry in the brittle crust and we seek the best possible fit to the data using a least-squares approach (see Methods).

In a first end-member model that is appropriate at conservative boundaries<sup>57,58</sup>, we assume that deformation concentrates in vertical shear zones ranging from the top of the lower crust to the bottom of the upper mantle, following CRUST1.0<sup>84</sup>. This model with homogeneous deformation in the crust and the upper mantle cannot fit the vertical and horizontal velocity fields simultaneously and is therefore discarded. In a second model, plastic deformation is entirely confined to the lower crust,

compatible with the typical strength profile of the continental lithosphere. This geometry produces a satisfactory fit to the data at the margin of the Tibetan Plateau, i.e., in regions of rapid uplift. However, the deformation around major strike-slip faults is severely underestimated, particularly next to the KLF and the XXF in northeast Tibet, around the central segment of the ATF between the Western Kunlun shan and the Qaidam Basin, and across the Sagaing Fault (SGF) in Myanmar. This indicates that the KLF, XXF, ATF, and SGF constitute trans-lithospheric structures akin to the San Andreas Fault in California<sup>57</sup> and the North Anatolian Fault in Turkey<sup>58</sup> that extend deep into the upper mantle. In our third and preferred model, we combine the positive aspects of the previous two ones. For the components of plastic strain rate leading to horizontal shear, the volume elements extend from the lower crust into the upper mantle, capturing faults or shear zones deep enough to offset the Mohorovičić (Moho) discontinuity<sup>87–89</sup> and their far-field displacement. For the remaining three components that lead to deformation along the vertical axis, the plastic strain rate is confined within the lower crust, resulting in a thickness of volume elements of 20–25 km in Tibet and of 5–10 km in the surrounding regions (Fig. S2).

**Kinematic model of the Indian–Eurasian collision.** Using regularized least squares and our preferred structural model, we invert the surface velocity field to estimate the spatial distribution of fault slip velocity and plastic strain rate. The inferred kinematic model (Figs. 2 and 3) reveals a wide collision zone ranging from the Himalayas to the Qilian shan and from the Tien shan to the Longmen shan. The most intense shortening concentrates along the periphery of the Tibetan Plateau, i.e., in the Himalayas, the Pamir, and the Tien shan regions, in a direction mostly perpendicular to the strike of local thrust faults (Figs. 2a and 3b), compatible with crustal thickening (Fig. 2b). The northern migration of the Indian continent is accommodated by much horizontal shear throughout the Indo-Burman ranges, and the most intense horizontal shear takes place around the SGF and in Pamir (Fig. 2c). In comparison, the regions of the ATF, KLF, XXF, and HYF faults may relate to horizontal pure shear with compaction and extension in orthogonal directions (Fig. 3). The intervening space of Central Tibet undergoes dominantly east-west extension (Fig. 2d), highlighting a latitudinal transition of strain orientation across the entire collision zone. The principal shortening direction in the Pamir-Tien shan is compatible with the oblique orientation of the orogenic belt relative to the Himalayan front. This rotation of the principal strain orientation may be explained by longitudinal forces exerted by the lateral extension of Central Tibet transmitted through a mostly rigid Tarim Basin. The inferred regions of crustal thickening and thinning are overall compatible with gravity measurements<sup>90</sup>, leveling data<sup>91</sup>, and seismic anisotropy<sup>92</sup>.

We illustrate the spatial resolution of the inversion based on a checkerboard test (Fig. S5), the spatial structure of the resolution matrix (Fig. S6), and the restitution index (Fig. S7). The sparse distribution of the geodetic stations and the filtering of the brittle crust limit the horizontal resolution to about 3°, with poor restitution of plastic strain rate near the boundaries of the model: in Northwest India, around the Chaman Fault (CMF), and east of the Sichuan Basin. In contrast, the components of horizontal strain are recovered well throughout most of the collision zone. With a limited number of geodetic stations with vertical measurements, we obtain a poor resolution of the vertical shear components of the plastic strain rate. However, the vertical uniaxial strain rate is well constrained due to the assumption of conservation of volume within the lower-crustal volume

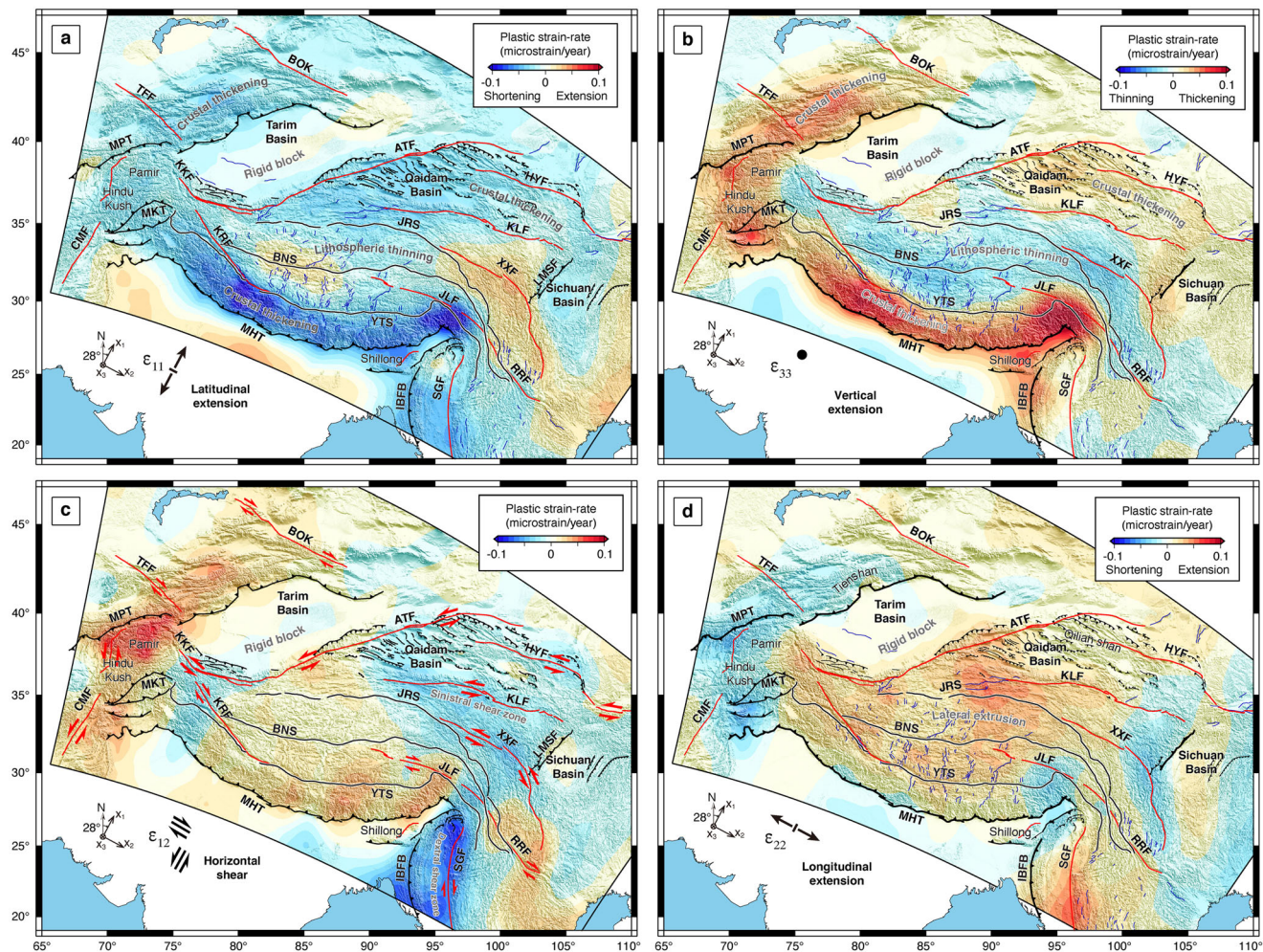


**Fig. 2 Kinematic model of the Indian-Eurasian collision zone.** The model<sup>134</sup> explains the geodetic data well, with a variance reduction of 88.2%, of which shallow faulting accounts for ~1% (Fig. S9). **a** Distribution of horizontal plastic strain-rate  $\epsilon_{11}$ , compatible with compression along the Indian-Eurasian convergence. **b** Vertical strain rate  $\epsilon_{33}$  in the lower crust, compatible with crustal thinning of Central Tibet and thickening of the collision margins. **c** Horizontal shear  $\epsilon_{12}$  being pronounced around the SGF and in Pamir. Negative  $\epsilon_{12}$  is compatible with north-south oriented dextral strike-slip faults (e.g., SGF) and with east-west oriented sinistral strike-slip faults (e.g., HYF, KLF, and XXF). **d** Strain-rate  $\epsilon_{22}$  indicating extension normal to the Indian-Eurasian convergence in the Tibetan Plateau.

elements: any horizontal shortening must be compensated exactly by a combination of orthogonal extension and uplift. The kinematic model explains the geodetic data well (Fig. S9), providing a variance reduction of 88.2%, a reduced chi-square of 1.48, and mean residual velocities of 0.93 mm/yr and 1.4 mm/yr in the horizontal and vertical directions, respectively. The modeled vertical velocities are also broadly consistent with the leveling measurements<sup>91</sup> (Fig. S10). The effect of fault motion in the brittle crust represents only about 1% of the variance reduction because faults, if not locked, only produce localized deformation during the interseismic period of the seismic cycle.

**Slip line field and tectonic regime of the Indian-Eurasian collision zone.** A conceptual explanation for the presence of continental-scale strike-slip faults in the Tibetan Plateau is the formation of slip lines behind a rigid indenter<sup>19,25,93–95</sup>. To explore this concept further, we evaluate the actual slip-line field for the Indian-Eurasian collision, exploiting the identical orientation of the plastic strain rate and the deviatoric stress—the stress tensor excluding the pressure—if related by an effective viscosity. Within this approximation, which applies in the absence of substantial plastic anisotropy, the plastic strain rate captures the

orientation of tectonic stress, i.e., of the full stress tensor minus the lithostatic pressure. The trajectories of two directions of maximum shear provide a set of two orthogonal slip lines associated with conjugate left-lateral and right-lateral faulting at any given location (Fig. 4a, b). Likewise, we generalize this concept for the maximum contraction and maximum extension, providing the overall orientation and spatial distribution of compressional and tensional strain (Fig. 4c, d).

Long segments of the left-lateral Chaman Fault (CMF), ATF, HYF, KLF, and XXF are closely aligned with one set of slip lines, while the right-lateral KRF, Boluokenu Fault (BOK), and SGF are closely aligned with the other one. Additionally, the majority of moment tensors for dominantly strike-slip historical earthquakes of moment magnitude 6.0 and above align with the slip lines. These results indicate the broad adequacy of the slip-line field model for the Tibetan Plateau, implying a low coefficient of friction of these mature faults, compatible with mechanical coupling between the brittle and ductile sections of the Tibetan crust.

In a similar manner, the trajectories of the principal contraction axis align perpendicular to the major thrust belts, along the Himalayas, the Hindu-Kush, Pamir, Tien shan, West

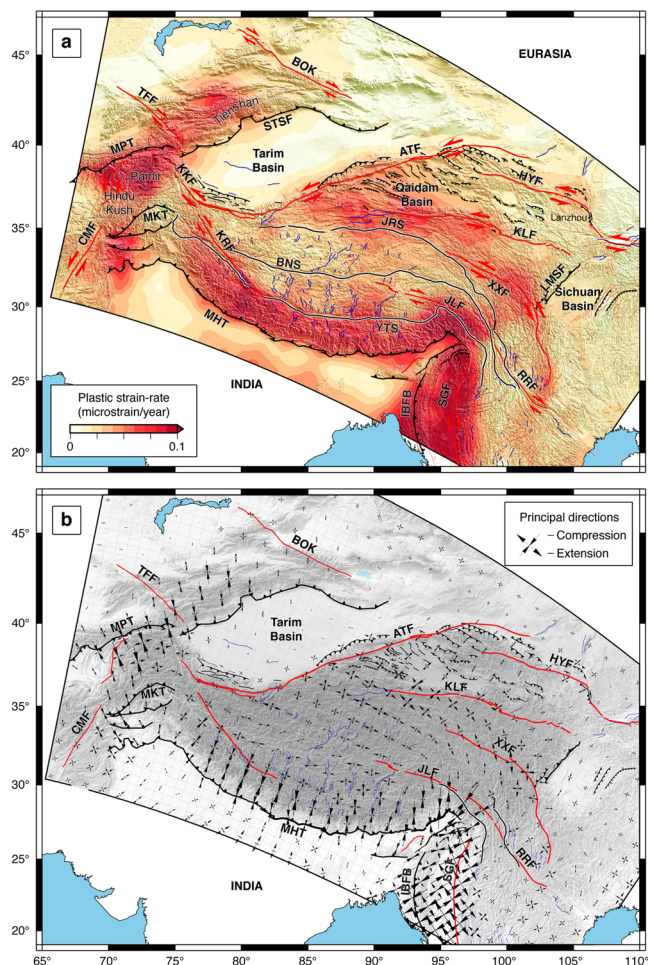


**Fig. 3** Inverted plastic strain rate. **a** Amplitude of the plastic strain-rate tensor. **b** Orientation of the horizontal principal strain-rate directions. The behavior of the vertical principal direction can be deduced by the conservation of volume—the trace of the plastic strain-rate tensor is zero.

Kunlun shan, East Kunlun shan, Qilian shan, Longmen shan, and Indo-Burman fold belt. Remarkably, the hypocenters of dominantly thrust earthquakes concentrate in the areas of large compressional strain, with moment tensors firmly aligned with the principal compressive strain direction. The spatial distribution of thrust and normal earthquakes is virtually complementary, with a majority of normal events concentrated in Central Tibet, between the Yarlung Tsangpo Suture (YTS) and the Jinsha Suture (JRS). The distribution of focal mechanisms gives credence to the distinct tectonic regimes of the Tibetan Plateau, with growth at the margins and thinning of the interior.

The spatial distributions of strain tensor in the lower crust can be characterized by the stress orientation factor that indicates regimes of dominant compression, shear, or extension as a scalar quantity (see Methods), again assuming a broad alignment between deviatoric stress and strain rate at these depths (Fig. 5). The diffuse collision zone is divided into broad regions of contraction and extension separated by narrow corridors of horizontal shear. The Tarim and Sihan Basins experience little strain rate and simply transmit the stress they experience at their boundary (Fig. 3). The southern and western borders of the collision zone, encompassing the Himalayas, Hindu-Kush, Pamir, and Tien shan, are dominated by compression, compatible with the surface structure of the Main Himalayan Thrust (MHT) and

the Pamir-Tien shan contraction belt that involve multiple thrust faults, e.g., the Main Pamir Thrust (MPT), Main Karakoram Thrust (MKT), and South Tien shan fault (STSF). The compressional regime of the northeastern border also coincides with the Longmen shan thrust and the Qilian shan. However, the presence of the sinistral ATF and HYF suggests the importance of slip partitioning with contraction within the Qilian shan and the Qaidam basin.

To the south, the transition from latitudinal compression to horizontal shear occurs near the YTS, above the northern termination of the Great Indian slab<sup>6</sup>. Farther north, Central Tibet showcases a ~300 km-wide extensional belt spanning over 2000 km from west to east centered along the BNS, coinciding with a dense field of rifts and grabens. Long segments of strike-slip faults, e.g., KLF, Red River Fault (RRF), Karakoram Fault (KRF), and the Sagaing Fault (SGF), as well as large parts of the ATF and XXF, spread over shear-dominated regions. The gradual rotation of the tectonic regime from compression at the margin to extension in the interior passing through an intermediate zone of horizontal shear appears to be a hallmark of the Indian-Eurasian collision zone.

**Rise and fall of the Tibetan Plateau.** Once calibrated to surface observations, geological structures, and earthquake distributions, the three-dimensional model allows examination of the vertical velocity field throughout the entire modeled region (Fig. 6). In a reference frame tied to Inner Mongolia, a broad subsiding region extends between the YTS and the JRS, from the western Kunlun shan to the Yunnan Province. The most rapidly subsiding region of the Tibetan Plateau is Central Tibet, coinciding with vertical thinning (Fig. 2b) and horizontal extension (Fig. 2d). The Tarim and Sichuan basins are also sinking, but mostly as rigid blocks, as evidenced by limited strain-rate in these regions (Fig. 3). The subsidence in Central Tibet is associated with the widespread rifting that accompanies escape tectonics<sup>14,15</sup>.

The rapid subsidence of the northern boundary of the Indian subcontinent is associated with the footwall of the Main Frontal Thrust that soles into the MHT<sup>96</sup>, but is a poorly resolved domain of the model. The subsidence of the western Sichuan basin, associated with the footwall of the Longmen Shan Fault (LMSF) is a more robust feature of the model. Subsidence of the Yunnan Province is found in an area of marked topographic gradient<sup>18</sup> and may occur to minimize gradients of gravitational potential energy<sup>37</sup>.

In contrast, crustal thickening is restricted to the margins of the Tibetan Plateau, in a continuous belt connecting the Himalayan, Hindu-Kush, Pamir, and Tien shan range and in a separate northern domain linking the Qaidam basin, the Qilian shan, and the Longmen shan (Fig. 6). When the diffuse plate boundary is considered in its wide ensemble, it is growing at its margins and subsiding in its interior in Central Tibet and the Tarim Basin.

**Subsurface kinematics.** Current understanding of the internal structure of the Indian-Eurasian collision zone relies extensively on seismic imaging of static structures within the lithosphere<sup>10,88,97–101</sup>. Complementing these techniques, the kinematic model allows us to reconstruct the subsurface velocity field and reveal the intricate interactions among the Indian, Tibetan, and Asian lithospheres. To visualize the internal deformation of the collision zone, we first compute the velocity field in the entire volume from the surface down to 160 km depth caused by the inferred plastic strain rate, encompassing the whole lithosphere. Next, we construct the streamlines of the surface velocity in map view (Fig. 7a) and the streamlines of the in-plane velocity field across longitudinal (Fig. 7b) and latitudinal profiles

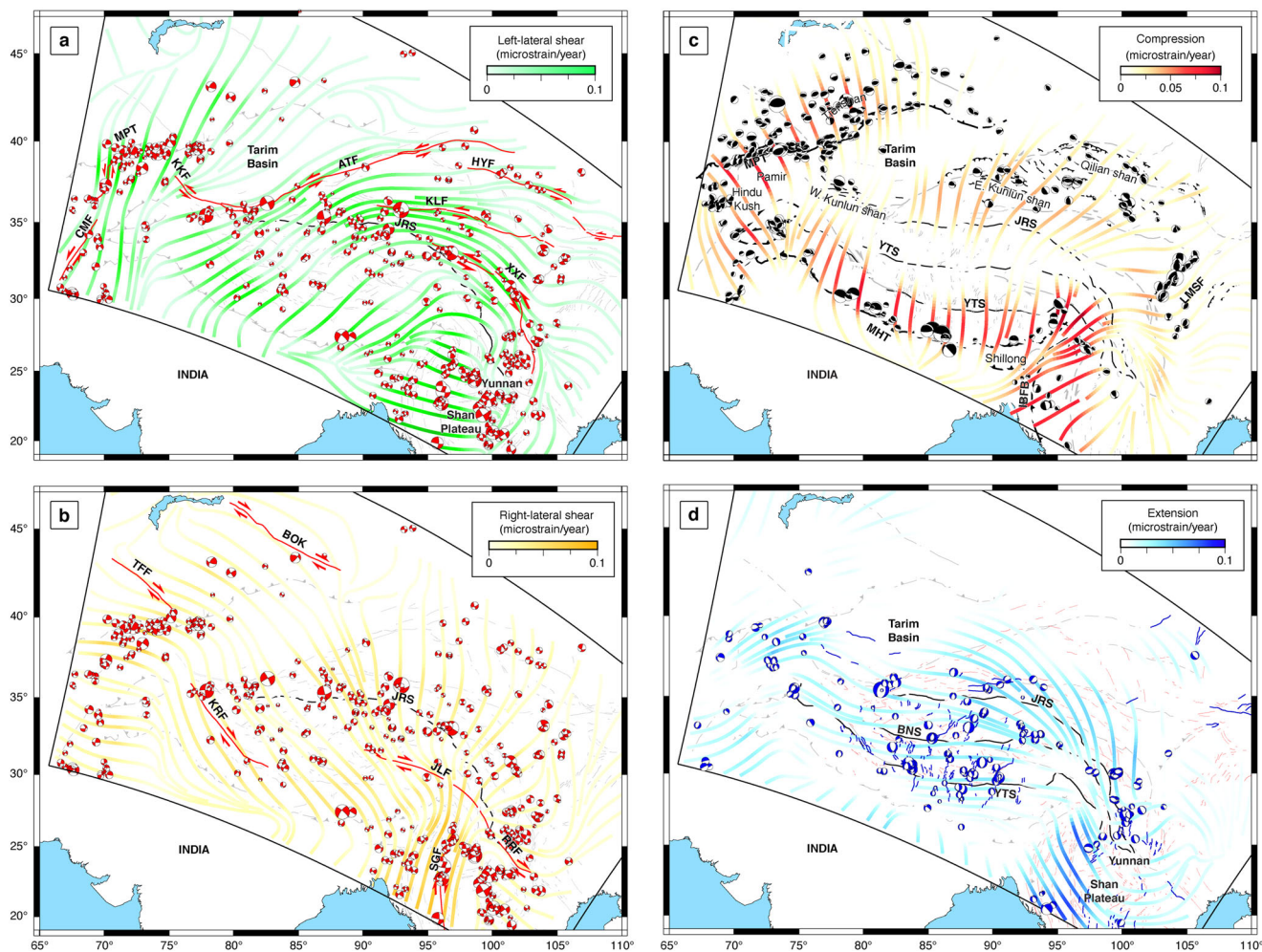


**Fig. 4** Slip-line field in the Indian-Eurasian collision zone built from plastic strain rate in the lower crust and upper mantle. **a** Layout of one set of slip lines built from the maximum shear of plastic strain rate, approaching the orientation of the ATF, HYF, KLF, XXF, and CMF left-lateral faults. **b** Orthogonal set of slip lines that matches the orientation of the KKF, SGF, TTF, and BOK right-lateral faults. The JLF and RRF are misoriented, compatible with their recent seismic quiescence. **c** Streamlines of horizontal compression, highlighting contractions at the margins of the collision zone, implying ongoing shortening. **d** Streamlines of horizontal extension, demonstrating large-scale extension within Central Tibet, the Yunnan province, and the Shan Plateau, compatible with the population of normal earthquakes. The beach balls indicate the focal mechanism of earthquakes of  $M_w \geq 6$  since 1970<sup>135</sup>, filtered by strike-slip (red), normal (blue), and thrust (black) mechanisms.

(Figs. 8 and 9). The streamlines represent the trajectory of crustal and mantle rocks as they traverse the plate boundary<sup>102</sup>, providing a useful proxy for regional kinematics. To facilitate the interpretation, the profiles are displayed in relation to the seismic velocity anomalies<sup>103</sup> and the surface and Moho topography<sup>84</sup>.

In map view (Fig. 7a), the deformation is dominated by a diverging flow-like motion that transports crustal and upper-mantle material to the east and west outlets of the diffuse plate boundary. The northern extension of the SGF is a singular point of concentrated rotation, as found at the termination of other major transform faults<sup>57,58</sup>. It is possible that similarly intense deformation takes place at the western syntaxis, at the northern termination of the CMF, but geodetic coverage is currently insufficient to resolve it (Figs. S5–S7).

The mechanics of escape tectonics within the collision zone can be further inferred from the longitudinal profiles (Fig. 7b), revealing the influence of material contrasts. The Tarim and Sichuan basins represent remnants of strong lithosphere incorporated into the plate boundary during the closure of the Tethys Ocean and behave as rigid blocks. Profiles N2 and N3, in combination with the streamlines in map view, reveal how lateral

extrusion circulates around these basins in three dimensions. The Tibetan rocks dive steeply as they approach the basins from the interior of the plateau, then flow horizontally in the upper mantle, and ascend on the other side. The horizontal flow in the Tarim and Sichuan upper mantles explains the spatial uniformity of the surface velocity field around these basins (Fig. 1a), implying that the strength of the basins only resides in their brittle section, while the Tarim, Sichuan, and Tibetan asthenospheres may have more uniform strengths. The resistance of the rigid crust of the Tarim and Sichuan basins apparently leads to material extrusion dominantly taking place south of these structures (Fig. 7a). The westward extrusion occurs between the Hindu-Kush subduction zone and the Main Pamir Thrust, leading to a rotation of the streamlines about the western syntaxis, a pattern compatible with seismic anisotropy<sup>104</sup>.

The morphology of the subducted Indian lithosphere varies greatly from west to east along the collision zone (Fig. 8). Across the Hindu-Kush and Pamir plateaus at the western syntaxis (profile P1), the Indian lithosphere or a short promontory directly collides with the Asian lithosphere below the MKT, at about 36°N. While crustal material is shortened and incorporated into

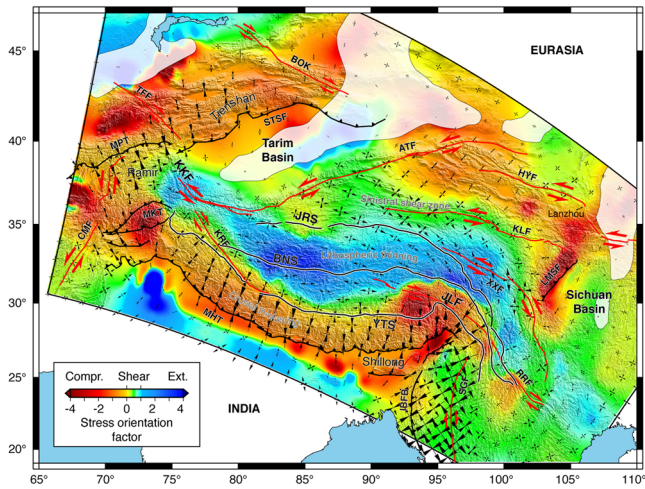


**Fig. 5** Stress orientation factor<sup>132</sup> illuminating the convergence belts at the plateau margins, the extensional belt in Central Tibet, and transitional shear regimes. The white-shaded areas of low strain-rate indicate unreliable estimates of the stress orientation factor. The pairs of arrows indicate the orientation of the deviatoric stress, in alignment with the horizontal principle strain.

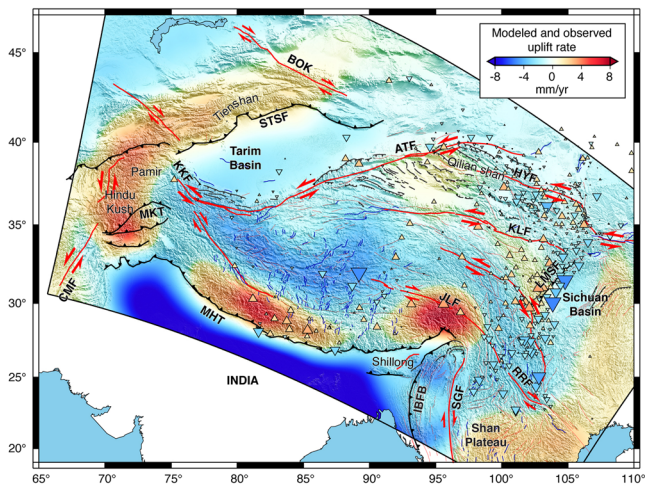


**Fig. 6** Rise and fall of the Tibetan Plateau. Modeled (background) and observed (triangles) rates of uplift and subsidence relative to the stable blocks northeast of the plateau<sup>63</sup>, indicating subsidence in Central Tibet and uplift at the southern and northeastern margins of the Tibetan Plateau and Pamir-Tien shan.

the Hindu-Kush and Pamir, the Indian and Eurasian mantles seem to detach and subduct, compatible with seismic tomography<sup>103,105–107</sup>, receiver functions<sup>108</sup>, and the locus of deep earthquakes<sup>109</sup> in this region. The orthogonal profile (N3) reveals that the east-west oriented collision takes place underneath the MPT, where the material extruded from the Tibetan Plateau encounters the Asian plate. Tearing of the Asian slab underneath the central Pamir may facilitate the westward extrusion of Tibetan material<sup>109</sup>.

Farther east, along the profiles P2 and P3 that cross the western Tarim basin, the Indian plate dives steeply south of the YTS, compatible with the regional P-wave radial anisotropy<sup>110</sup>. Along the profiles, P4 and P5 that cross the eastern Tarim Basin, the Indian lithosphere splits into a crustal sliver that thickens the Himalayas and the remaining mantle that dives steeply

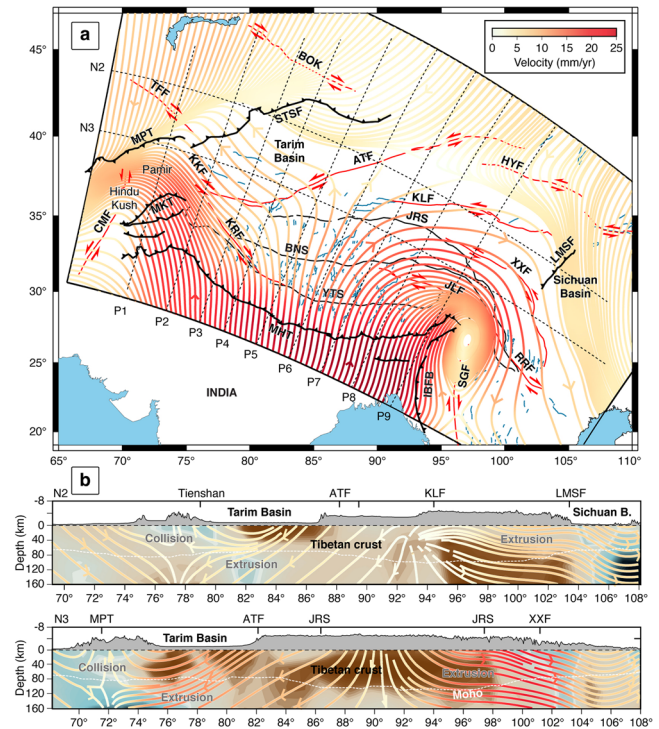


**Fig. 7** Horizontal and longitudinal kinematics of the Indian-Eurasian collision zone. **a** Streamlines of horizontal flow in the lower crust showing the convergence of the Indian slab as far north as the YTS, transitioning to lateral escape north of the BNS. Converging streamlines indicate contraction; diverging lines indicate horizontal extension. Large grabens concentrate at the pivot line of lateral extrusion in Central Tibet. Flow in Indochina is dominated by outward diverging motion. **b** Longitudinal velocity profiles N2 & N3 (see map A for location) across the Indian-Eurasian diffuse plate boundary, capturing convergence below the Tien shan, overall lateral extrusion of the Tibetan lithosphere, and horizontal flow below the Tarim and Sichuan basins. The line color indicates the in-plane velocity. The thin white line shows the depth of the Moho from CRUST1.0<sup>84</sup>. The background color map in (b) indicates the seismic tomography<sup>103</sup>.

underneath, south of the KRF. At this longitude, the Indian crust and upper mantle showcase a strongly diverging trajectory between 30° and 32°N, indicative of delamination rollback of the Indian mantle<sup>9–11</sup> and crustal shortening with thrust faulting and folding. The change of overall kinematics that occurs in Central Tibet between profiles P4 and P5 coincides with a transition to a much thickened Tibetan crust in seismic tomography<sup>103</sup>.

Along the central profile P6 (Fig. 9), delamination is diminished, possibly supplanted by the injection of continental crust below and across the YTS, which is suggested by the flatter trajectory of the Indian crust. At this position along the Himalayan Arc, the Indian mantle continues down on a more gentle plunge, following a ramp-flat-ramp sequence of lithospheric proportions. Along the profiles P7 and P8 that cross the KLF, the ATF, and the Qaidam basin, continental underthrusting of the Indian lithosphere below Southern Tibet as a whole can be recognized as upper mantle rocks traverse the Tibetan Plateau at low angle or sub-horizontally. The transition from steep to more gentle subduction of the Indian mantle (from profile P5 to P7) corresponds to the pivot of tectonic extrusion and a greater density of rift zones. Close to the eastern syntaxis, along profile P9, crustal shortening with a possible injection of Indian crust resumes below the YTS even though the Indian mantle continues

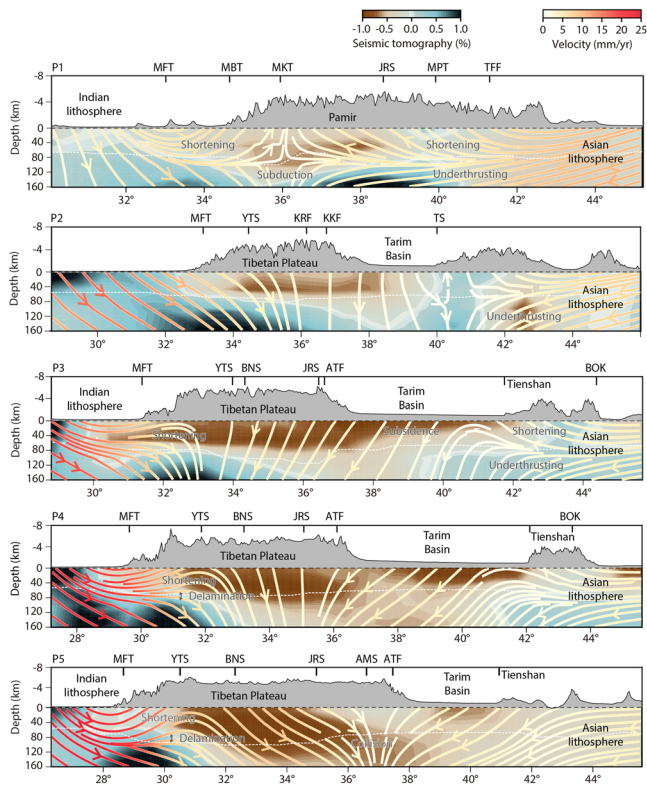


**Fig. 8 Latitudinal kinematics of the western Indian-Eurasian collision zone.** Latitudinal velocity profiles P1–P5 (see map A of 7 for location) across the Indian–Eurasian diffuse plate boundary, compatible with crustal shortening and delamination rollback near the western syntaxis and continental underthrusting in the Central Himalayas. The Asian lithosphere transitions from deep subduction below the Hindu-Kush and Pamir to the west (profile P1) to continental underthrusting below the Tarim basin in profiles P2 to P5. The line color indicates the in-plane velocity. The thin white line shows the depth of the crust–mantle (Moho) boundary from CRUST1.0<sup>84</sup>. The background color map indicates the seismic tomography<sup>103</sup>. The MFT and MBT faults sole into the MHT that forms the basal décollement below the Himalayan orogenic wedge.

its gentle dive. Along profiles P5 to P9, the inferred collision zone between the Indian and Asian lithosphere coincides with the low-velocity anomaly associated with the Tibetan lithosphere<sup>103</sup>.

The southern boundary of the Asian lithosphere also varies greatly along the margin. Subduction of the Asian lithosphere takes place below Pamir in profile P1 by underthrusting starting from north of the Talas–Fergana Fault (TFF) in the Kyrgyz (northern) Tien shan, compatible with geological interpretations<sup>111</sup>. Much crustal material is assimilated into the Pamir edifice, culminating with steeper subduction at 36°N. Farther east, the southward motion of Asia is obstructed by the harder or denser volume below Tianshan and Tarim Basin, as suggested by seismic velocity structure<sup>103</sup>, the convergence is slower, and the collision setting differs greatly. Along profiles P3 and P4, the Asian crust is shortened below the Tien shan and the Asian mantle steeply dives below the northern margin of the Tarim Basin, in almost symmetry with the Indian lithosphere below the MHT across the Tibetan Plateau. East of the Tarim Basin, the ATF and its relay with the HYF constitute the collision front between Tibet and the Asian plate. Along profiles P7 and P8, the Asian lithosphere subducts gently below the Qaidam Basin and the Qilian shan, compatible with seismic imaging with receiver functions<sup>112</sup>. While crustal thinning and material extrusion related to subsidence dominate in and around Central

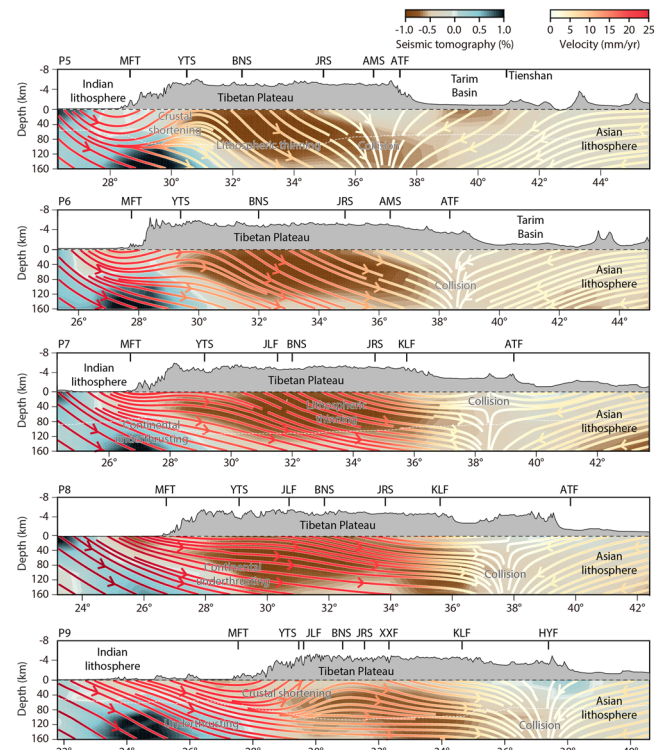


**Fig. 9 Latitudinal kinematics of the eastern Indian-Eurasian collision zone.** Latitudinal velocity profiles P5–P9 (see map A of 7 for location) across the Indian–Eurasian diffuse plate boundary, showing crustal shortening and delamination rollback in profile P5 transitioning to continental underthrusting in the Central Himalayas towards the eastern syntaxis in profiles P6 to P9. The collision between the Tibetan and Asian lithospheres occurs at about 38°N. The line color indicates the in-plane velocity. The thin white line shows the depth of the crust–mantle (Moho) boundary from CRUST1.0<sup>84</sup>. The background color map indicates the seismic tomography<sup>103</sup>.

Tibet (profiles P3 to P8), in concert with subduction on the northern and southern sides, crustal shortening and surface uplift dominate near the western and eastern syntaxes.

**Tectonic assembly of the collision zone.** Several mechanisms of growth of the Tibetan Plateau have been proposed, including continental underthrusting<sup>1,2</sup>, convective removal of the base of the lithosphere<sup>35</sup>, distributed thickening by indentation of stronger Indian lithosphere<sup>113</sup>, flow within a narrow channel near the base of the crust<sup>8,114</sup>, delamination of the upper mantle with injection of lower-crustal material<sup>8–11</sup>, northward retreat and migration of successive Asian collision zones with internal sedimentation<sup>13,115</sup>, and accretion of several continental blocks along major sutures<sup>29,116,117</sup>. Meanwhile, the thinning of the lithosphere in Central Tibet implied by widespread rifting has been firmly recognized<sup>14,15,20</sup>. In all likelihood, a combination of mechanisms in space and time may be involved rather than a single one, and whether and how the present-day Tibetan Plateau is rising and falling remains elusive<sup>42</sup>.

Our three-dimensional kinematic model of the Indian–Eurasian collision provides new constraints on subsurface kinematics, highlighting the spatial arrangement of large-scale tectonic processes (Fig. 10). Uplift at the southern margin is caused by underthrusting of the Indian mantle and shortening of the overriding crust. Although limited to the south of the BNS in most places, flat underthrusting by the Indian mantle may reach



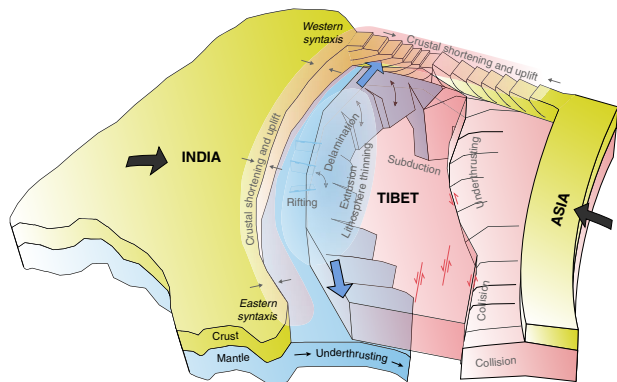


**Fig. 10 Tectonic assembly of the Indian-Eurasian collision with patterns of uplift and subsidence.** A direct collision between the Indian and Asian lithospheres occurs near the western syntaxes. Delamination of the Indian lithosphere takes place along the western section of the Himalayan arc. Underthrusting of the Indian mantle below the Tibetan Plateau can be found from the central to eastern Himalayas. Lateral escape and lithosphere thinning are accommodated by rifting and trans-lithospheric faults. The Tibetan Plateau is growing at its margins and subsiding in its interior in Central Tibet.

as far north as the JRS in eastern Tibet. Our analysis shows evidence of delamination of the Indian plate from the western syntaxis to the KRF. However, we cannot find strong evidence for the injection of crustal material into Tibet and we also lack the resolution to infer convection patterns within the Tibetan asthenosphere. The growth of the eastern and northeastern Tibetan Plateau is caused by the assimilation of Indian crustal material near the eastern syntaxis, by the bulging of the Tibetan crust against the Sichuan basin east of the Songpan-Ganzi terrane, and by crustal shortening within the Tibetan-Asian collision around the Qaidam basin and the Qilian shan.

In contrast, Central Tibet is subsiding relative to a tectonically stable block in Inner Mongolia, which may be surprising in the context of a continental collision. Local east-west extension across the YTS could be related to the diverging motion of the south-vergent Himalayan megathrust<sup>15</sup>. However, the wide subsidence of Central Tibet across the BNS and as far north as the JRS indicates a broader geodynamic origin. More likely, subsidence results from the dominance of far-field boundary conditions, namely the large gradients of gravitational potential energy in the Yunnan Province and the Shan Plateau<sup>18</sup> assisted by slab retreat at the Sunda and Western Pacific subduction zones<sup>21,22</sup>. Additional deflation with limited internal strain within the plateau may come from deep downwelling currents or a flexure induced by the subducting and opposite-facing Indian and Asian slabs, explaining the descent of the Tarim basin as a virtually rigid block. In Central Tibet, the subsidence is accommodated by active rifting, which may extend throughout the entire lithosphere, as evidenced by large-scale S-wave velocity anomalies beneath the Tangra Yum Co, Yadong-Gulu, and Cona rifts<sup>118</sup>. The lateral extension and lithospheric thinning of South Tibet may interact with the Indian mantle below the YTS, possibly causing multiple slab tears that allow the lateral transition from collision to more gentle subduction that plays out along the Himalayan arc<sup>88,101,119</sup>.

The contemporaneous subsidence of Central Tibet is confirmed by independent estimates of vertical displacements from geodetic measurements and gravity changes<sup>90,91,120</sup>, as well as seismic anisotropy<sup>92</sup>, but similar patterns of uplift and subsidence may have operated since the middle Miocene<sup>26</sup>. The Oiyug Basin, located on the Lhasa terrane about 160 km west of Lhasa and

60 km north of the YTS shows a possible 1 km decrease in elevation since the early Pliocene<sup>121</sup>. This is corroborated by a nearby study of fossil floras in the Namling-Oiyug Basin that suggests a 1 km deflation since the middle Miocene<sup>122</sup>. Farther to the west, the Zhada Basin, which abuts the YTS at 31°N-80°E, shows evidence for a peak elevation up to 1.5 km higher than today during the Miocene<sup>123</sup>. In the Tarim Basin, oxygen isotope data reveal a negative isotopic shift in the Miocene strata compatible with subsidence of the basin relative to the nearby Tien shan<sup>124</sup>. This is in contrast to other sites in northeastern Tibet and the Himalayas showing crustal thickening or stable elevation for a substantial period<sup>125,126</sup>. The current mobilization of multiple end-member mechanisms of growth and subsidence may reflect the differential evolution of the inner and outer Tibetan Plateau during the late Cenozoic.

Our study reveals a differential pattern of uplift and subsidence in the Tibetan Plateau accompanied by marked differences in subsurface geometry of the Indian and Asian slabs and finite rotation of the principal strain from compression at the margins to lateral extension in the interior. The kinematic model is compatible with an outward growth of the Tibetan Plateau during the Cenozoic with in-filling of its interior by sedimentation and bilateral extrusion of the Tibetan lithosphere accommodated by deep-rooted rifts and trans-lithospheric transform faults. Kinematic models of lithospheric deformation that assimilate brittle and ductile processes illuminate the broad pattern of internal deformation at active margins, complementing seismic imaging with tomography or receiver functions.

## Methods

**Geodetic velocity field.** We assemble available GNSS data from multiple networks and studies. The majority of the data are from the Crustal Movement Observation Network of China (CMONOC) that operates since 1998<sup>17,54</sup>. We also incorporate GNSS data from the Global Strain Rate Model<sup>59</sup> and several regional networks in the Indo-Burman ranges<sup>60</sup>, the Pamir plateau<sup>61</sup>, and the Tien shan<sup>62</sup>, leading to 2870 horizontal velocity measurements. All these data are unified into a stable Eurasia reference frame via aligning the common stations. We also include 450 vertical GNSS measurements<sup>63</sup> expressed relative to three stable sites northeast of the Tibetan Plateau, which are distributed about 800 km apart and have reliable vertical velocity estimations with observation time span over 12 years. These GNSS measurements may represent secular plate motion and deformation because time series data for constructing the velocity field had been selected to circumvent the earthquakes.

The velocity field presented in Fig. 1 is free of any net rotation, which we derive as follows. Any rigid motion at the surface of the Earth can be represented by a rotation about an Euler pole. The velocity field caused by the rotation about any arbitrary Euler pole can be decomposed as the linear combination of three individual rotations about Euler poles situated at 1) the North pole, 2) along the equator at the Greenwich Meridian, and 3) 90° farther east, respectively. If the spin rate about each Euler pole is written  $\omega_i$ ,  $i = 1, 2, 3$ , the velocity at a station location at longitude  $\phi$  and latitude  $\theta$  is given by

$$\begin{bmatrix} V_N \\ V_E \end{bmatrix} = R \begin{bmatrix} \sin \theta & -\cos \phi & 0 \\ -\sin \theta \cos \phi & -\sin \phi \sin \theta & \cos \theta \end{bmatrix} \begin{bmatrix} \omega_1 \\ \omega_2 \\ \omega_3 \end{bmatrix} \quad (1)$$

where  $R$  is the local radius of the Earth and  $V_N$  and  $V_E$  are the north and east components of the horizontal velocity vector (Fig. S1). To remove overall translation and rotation from the velocity field so that the local deformation can be secluded from the adopted reference system, we obtain the coefficient  $\omega_i$  by least-squares fitting. We express the vertical component of the velocity field relative to the average vertical displacement at stations DXIN, YANG, and ULAB located northeast of the plateau in Inner Mongolia.

**Geodetic inverse problem.** According to a stratified lithosphere rheology<sup>86</sup>, we assume that the tectonic component of surface deformation is caused by the accumulation of plastic strain in the lower crust and upper mantle, and slip on major thrusts—MHT, IBFB, LMSF, STSF, MKT, MPT, and several others around the western syntaxis—and major strike-slip faults (CMF, JLF, KLF, ATF, HYF, XXF, BOK, TFF, RRF, SGF, and KKF) that operating in the brittle layer of the crust. Such a stratified modeling strategy is different from rigid block model which treats the lithosphere as an elastic unit<sup>88,51,127</sup>. In alignment with the surface fault traces, we consider vertical planes for strike-slip faults and oblique planes for thrust faults constrained by geological and seismological data, and discretize the faults

with triangle elements from the local seismogenic layer to the brittle-ductile transition provided by CRUST1.0<sup>84</sup>. However, we allow shallow slip on the HYF, for which surface creep has been captured<sup>128</sup>. We discretize the underlying ductile regime with a rectilinear mesh (Fig. S2). The surface velocity is due to a linear combination of slip on surface elements, strain in volume elements, rotation about an unknown Euler pole, and unknown vertical offset relative to the reference frame. This is captured by a linear system that relates  $\mathbf{d}$ , the data vector, to the unknown parameters via a design matrix, as

$$\mathbf{d} = [\mathbf{G}_s \quad \mathbf{G}_\epsilon \quad \mathbf{G}_\omega \quad \mathbf{G}_z] \begin{bmatrix} \mathbf{s} \\ \boldsymbol{\epsilon} \\ \boldsymbol{\omega} \\ d_z \end{bmatrix} \quad (2)$$

where  $\mathbf{s}$  represents slip on faults,  $\boldsymbol{\epsilon}$  are the six components of the plastic strain-rate tensor,  $\boldsymbol{\omega}$  is the spin rate along three independent rotation axes, and  $d_z$  is the regional mean uplift rate in the reference frame of the data. The design matrix  $\mathbf{G} = [\mathbf{G}_s, \mathbf{G}_\epsilon, \mathbf{G}_\omega, \mathbf{G}_z]$  is composed of the Green's functions for fault slip<sup>129</sup>, plastic strain<sup>130,131</sup>, rotations, and uniform uplift, respectively.

We build a rectilinear mesh of the region with  $63 \times 36$  volume elements of 70 km length aligned in the convergence direction N28°E (Fig. S2). Examples of columns of the Green's functions  $\mathbf{G}_\epsilon$  are shown in map view in Figs. S3 and S4. We obtain the best-fitting distribution of fault slip and lower-crustal and upper-mantle strain-rate by a regularized least-squares inversion with Laplacian smoothing. Further technical details can be found in previous work<sup>57,58</sup>. We use non-negative constraints for fault creep to enforce slip in the direction of long-term fault motion. We also enforce deviatoric plastic strain to conserve mass in the lithosphere.

To inspect the properties of the inverse problem, we build a checkerboard test (Fig. S5) and inspect the resolution matrix  $\mathbf{R} = \mathbf{G}^\dagger \mathbf{G}$ , where  $\mathbf{G}^\dagger$  is the Moore-Penrose pseudo inverse of  $\mathbf{G}$ . The trace of the diagonal of the resolution matrix indicates the number of well-constrained model parameters. Diagonal elements much lower than unity point to low resolution. The resolution is high for the three horizontal strain components and the uni-axial vertical strain component, but poor for the vertical shear (Fig. S6). The spatial filtering of the recovered spike models contained as column-vector of  $\mathbf{R}$  (Fig. S8) indicates a variable spatial resolution of 1–3°, commensurate with the size of 3 to 6 adjacent volume elements, depending on the measurement density at the surface. The restitution index evaluated by the sum of the rows of  $\mathbf{R}$  reflects whether a single strain component is recovered by the whole observation network (Fig. S7). Overall the uni-axial and horizontal pure-shear components are well constrained, except at the margins of the model, i.e., south of the MHT and south of the western Himalayan syntaxis.

**Stress orientation factor.** The stress orientation factor, defined as

$$r = \frac{\sigma_z - \sigma_x}{\sigma_y - \sigma_x}, \quad (3)$$

with  $\sigma_y > \sigma_x$  and  $\sigma_z$  being the principal stress closest to the vertical<sup>132</sup>, is a scalar quantity documenting the regime of the tectonic stress. Values  $r \in [-\alpha$  to 0] correspond to horizontal compression,  $r \in [0-1]$  indicates horizontal shear compatible with strike-slip faulting, and  $r \in [1-\infty]$  corresponds to horizontal extension. We calculate the stress orientation factor for the Indian-Eurasian collision zone using the inferred plastic strain-rate tensor (Fig. 2e), exploiting the alignment of the deviatoric stress and the plastic-strain rate in the ductile domain.

## Data availability

Part of GPS velocity data are from [GSRM project](#). The data of crustal thickness are from CRUST1.0. The data of seismic tomography are from [SubMachine](#). The compiled GPS data and the produced plastic strain rate are available from [https://doi.org/10.5281/zenodo.7771626\(3D-India-Eurasia-collision\)](https://doi.org/10.5281/zenodo.7771626(3D-India-Eurasia-collision)).

## Code availability

The code used for this study can be accessed at <https://bitbucket.org/sbarbot/bssa-2016237/>.

Received: 26 August 2022; Accepted: 21 April 2023;

Published online: 12 May 2023

## References

- Argand, E. La tectonique de l'Asie. In: Proc. 13th Geological Congress Belgique, Comptes Rendus **1**, 171–372 (1922).
- Powell, C. M. & Conaghan, P. Plate tectonics and the Himalayas. *Earth Planet. Sci. Lett.* **20**, 1–12 (1973).
- Zhao, W.-L. & Morgan, W. J. Injection of Indian crust into Tibetan lower crust: a two-dimensional finite element model study. *Tectonics* **6**, 489–504 (1987).
- Kosarev, G. et al. Seismic evidence for a detached Indian lithospheric mantle beneath Tibet. *Science* **283**, 1306–1309 (1999).
- Tilmann, F., Ni, J. & INDEPTH III, S. T. Seismic imaging of the downwelling Indian lithosphere beneath central Tibet. *Science* **300**, 1424–1427 (2003).
- Nábělek, J. et al. Underplating in the Himalaya-Tibet collision zone revealed by the Hi-CLIMB experiment. *Science* **325**, 1371–1374 (2009).
- DeCelles, P. G., Robinson, D. M. & Zandt, G. Implications of shortening in the Himalayan fold-thrust belt for uplift of the Tibetan Plateau. *Tectonics* **21**, 12–1 (2002).
- Zhao, W.-L. & Morgan, W. J. Injection of Indian crust into Tibetan lower crust: a two-dimensional finite element model study. *Tectonics* **6**, 489–504 (1987).
- Harrison, T. M., Copeland, P., Kidd, W. & Yin, A. Raising Tibet. *Science* **255**, 1663–1670 (1992).
- Zhang, Z. et al. Geophysical constraints on the link between cratonization and orogeny: evidence from the Tibetan Plateau and the North China Craton. *Earth-Science Rev.* **130**, 1–48 (2014).
- Shi, D. et al. Receiver function imaging of crustal suture, steep subduction, and mantle wedge in the eastern India–Tibet continental collision zone. *Earth Planet. Sci. Lett.* **414**, 6–15 (2015).
- Roger, F. et al. An Eocene magmatic belt across central Tibet: mantle subduction triggered by the Indian collision? *Terra Nova* **12**, 102–108 (2000).
- Tapponnier, P. et al. Oblique stepwise rise and growth of the Tibet plateau. *Science* **294**, 1671–1677 (2001).
- Armijo, R., Tapponnier, P., Mercier, J. & Han, T.-L. Quaternary extension in southern Tibet: Field observations and tectonic implications. *J. Geophys. Res.* **91**, 13803–13872 (1986).
- Chevalier, M.-L. et al. Late quaternary extension rates across the northern half of the Yadong-Gulu Rift: implication for east-west extension in Southern Tibet. *J. Geophys. Res.* **125**, e2019JB019106 (2020).
- Tapponnier, P. & Molnar, P. Active faulting and tectonics in China. *J. Geophys. Res.* **82**, 2905–2930 (1977).
- Wang, M. & Shen, Z.-K. Present-day crustal deformation of continental China derived from GPS and its tectonic implications. *J. Geophys. Res.* **125**, e2019JB018774 (2020).
- Clark, M. K. & Royden, L. H. Topographic ooze: Building the eastern margin of Tibet by lower crustal flow. *Geology* **28**, 703–706 (2000).
- Tapponnier, P., Peltzer, G., Le Dain, A., Armijo, R. & Cobbold, P. Propagating extrusion tectonics in Asia: New insights from simple experiments with plasticine. *Geology* **10**, 611–616 (1982).
- Yin, A. Mode of Cenozoic east-west extension in Tibet suggesting a common origin of rifts in Asia during the Indo-Asian collision. *J. Geophys. Res.* **105**, 21745–21759 (2000).
- Schellart, W., Chen, Z., Strak, V., Duarte, J. & Rosas, F. Pacific subduction control on Asian continental deformation including Tibetan extension and eastward extrusion tectonics. *Nat. Commun.* **10**, 1–15 (2019).
- Bose, S., Schellart, W. P., Strak, V., Duarte, J. C. & Chen, Z. Sunda subduction drives ongoing India-Asia convergence. *Tectonophysics* 229727 <https://www.sciencedirect.com/science/article/pii/S0040195123000252> (2023).
- England, P. & Houseman, G. Role of lithospheric strength heterogeneities in the tectonics of Tibet and neighbouring regions. *Nature* **315**, 297–301 (1985).
- Molnar, P. & Tapponnier, P. Cenozoic tectonics of Asia: effects of a continental collision. *Science* **189**, 419–426 (1975).
- Tapponnier, P. & Molnar, P. Slip-line field theory and large-scale continental tectonics. *Nature* **264**, 319–324 (1976).
- Searle, M. The rise and fall of Tibet. *Nature* **374**, 17–18 (1995).
- Searle, M. P., Elliott, J. R., Phillips, R. J. & Chung, S.-L. Crustal-lithospheric structure and continental extrusion of Tibet. *J. Geol. Soc.* **168**, 633–672 (2011).
- Cai, F., Ding, L. & Yue, Y. Provenance analysis of upper Cretaceous strata in the Tethys Himalaya, southern Tibet: implications for timing of India-Asia collision. *Earth Planet. Sci. Lett.* **305**, 195–206 (2011).
- Pan, G. et al. Tectonic evolution of the Qinghai-Tibet plateau. *J. Asian Earth Sci.* **53**, 3–14 (2012).
- Kapp, P. & DeCelles, P. G. Mesozoic-Cenozoic geological evolution of the Himalayan-Tibetan orogen and working tectonic hypotheses. *Am. J. Sci.* **319**, 159 LP – 254 (2019).
- Su, T. et al. No high Tibetan Plateau until the Neogene. *Sci. Adv.* **5**, eaav2189 (2019).
- Kelly, S., Beaumont, C. & Butler, J. P. Inherited terrane properties explain enigmatic post-collisional Himalayan-Tibetan evolution. *Geology* **48**, 8–14 (2019).
- Hu, F. et al. Quantitatively tracking the elevation of the Tibetan Plateau since the Cretaceous: insights from whole-rock Sr/Y and La/Yb ratios. *Geophys. Res. Lett.* **47**, e2020GL089202 (2020).
- Taylor, M., Forte, A., Laskowski, A. & Ding, L. Active uplift of southern Tibet revealed. *GSA Today* **31** <https://par.nsf.gov/biblio/10273400> (2021).
- England, P. C. & Houseman, G. The mechanics of the Tibetan Plateau. *Philos. Trans. R. Soc. Lond. Series A, Math. Phys. Sci.* **326**, 301–320 (1988).

36. England, P. C. & Molnar, P. Active deformation of Asia: from kinematics to dynamics. *Science* **278**, 647–650 (1997).
37. Bischoff, S. H. & Flesch, L. M. Normal faulting and viscous buckling in the Tibetan Plateau induced by a weak lower crust. *Nat. Commun.* **9**, 1–9 (2018).
38. Bendick, R. & Flesch, L. Reconciling lithospheric deformation and lower crustal flow beneath central Tibet. *Geology* **35**, 895–898 (2007).
39. Capitanio, F. A. Current deformation in the Tibetan Plateau: a stress gauge in the India-Asia collision tectonics. *Geochem. Geophys. Geosyst.* **21**, e2019GC008649 (2020).
40. Chen, L., Capitanio, F. A., Liu, L. & Gerya, T. V. Crustal rheology controls on the Tibetan plateau formation during India-Asia convergence. *Nat. Commun.* **8**, 15992 (2017).
41. Huangfu, P., Li, Z.-H., Fan, W., Zhang, K.-J. & Shi, Y. Continental lithospheric-scale subduction versus crustal-scale underthrusting in the collision zone: numerical modeling. *Tectonophysics* **757**, 68–87 (2019).
42. Ding, L. et al. Timing and mechanisms of Tibetan Plateau uplift. *Nat. Rev. Earth Environ.* **3**, 652–667 (2022).
43. Holt, W. et al. Velocity field in Asia inferred from Quaternary fault slip rates and Global Positioning System observations. *J. Geophys. Res.* **105**, 19185–19209 (2000).
44. Zhang, P.-Z. et al. Continuous deformation of the Tibetan plateau from global positioning system data. *Geology* **32**, 809–812 (2004).
45. England, P. & Molnar, P. Late Quaternary to decadal velocity fields in Asia. *J. Geophys. Res.* **110**, B12401 (2005).
46. Gan, W. et al. Present-day crustal motion within the Tibetan Plateau inferred from GPS measurements. *J. Geophys. Res.* **112**, B08416 (2007).
47. Avouac, J. P. & Tapponnier, P. Kinematic model of active deformation in central Asia. *Geophys. Res. Lett.* **20**, 895–898 (1993).
48. Loveless, J. P. & Meade, B. J. Partitioning of localized and diffuse deformation in the Tibetan Plateau from joint inversions of geologic and geodetic observations. *Earth Planet. Sci. Lett.* **303**, 11–24 (2011).
49. Langstaff, M. A. & Meade, B. J. Edge-driven mechanical microplate models of strike-slip faulting in the Tibetan plateau. *J. Geophys. Res. Solid Earth* **118**, 3809–3819 (2013).
50. Zhang, Z., McCaffrey, R. & Zhang, P. Relative motion across the eastern Tibetan plateau: contributions from faulting, internal strain and rotation rates. *Tectonophysics* **584**, 240–256 (2013).
51. Wang, Y., Wang, M. & Shen, Z.-K. Block-like versus distributed crustal deformation around the northeastern Tibetan plateau. *J. Asian Earth Sci.* **140**, 31–47 (2017).
52. Jian, H., Gong, W., Li, Y. & Wang, L. Bayesian inference of fault slip and coupling along the Tuosuo Lake segment of the Kunlun fault, China. *Geophys. Res. Lett.* **49**, e2021GL096882 (2022).
53. Ader, T., Avouac, J. P., Liu-Zeng, J., Lyon-Caen, H. & Bollinger, L. Convergence rate across the Nepal Himalaya and interseismic coupling on the Main Himalayan Thrust: implications for seismic hazard. *J. Geophys. Res.* **117**, B04403 (2012).
54. Zheng, G. et al. Crustal deformation in the India-Eurasia collision zone from 25 Years of GPS measurements. *J. Geophys. Res. Solid Earth* **122**, 9290–9312 (2017).
55. Qiu, Q., Moore, J. D. P., Barbot, S., Feng, L. & Hill, E. Transient rheology of the Sumatran mantle wedge revealed by a decade of great earthquakes. *Nat. Commun.* **9**, 995 (2018).
56. Tang, C.-H., Hsu, Y.-J., Barbot, S., Moore, J. D. P. & Chang, W.-L. Lower-crustal rheology and thermal gradient in the Taiwan orogenic belt illuminated by the 1999 Chi-Chi earthquake. *Sci. Adv.* **5**, eaav3287 (2019).
57. Barbot, S. Mantle flow distribution beneath the California margin. *Nat. Commun.* **11**, 1–14 (2020).
58. Barbot, S. & Weiss, J. Connecting subduction, extension and shear localization across the Aegean Sea and Anatolia. *Geophys. J. Int.* **226**, 422–445 (2021).
59. Blewitt, G., Kreemer, C., Hammond, W. C. & Gazeaux, J. MIDAS robust trend estimator for accurate GPS station velocities without step detection. *J. Geophys. Res.* **121**, 2054–2068 (2016).
60. Steckler, M. S. et al. Locked and loading megathrust linked to active subduction beneath the Indo-Burman Ranges. *Nat. Geosci.* **9**, 615–618 (2016).
61. Zhou, Y. et al. Present-day crustal motion around the Pamir Plateau from GPS measurements. *Gondwana Res.* **35**, 144–154 (2016).
62. Pan, Y. et al. Contemporary mountain-building of the tianshan and its relevance to geodynamics constrained by integrating GPS and GRACE measurements. *J. Geophys. Res. Solid Earth* **124**, 12171–12188 (2019).
63. Liang, S. et al. Three-dimensional velocity field of present-day crustal motion of the Tibetan Plateau derived from GPS measurements. *J. Geophys. Res.* **118**, 5722–5732 (2013).
64. Pan, Y., Shen, W.-B., Shum, C. & Chen, R. Spatially varying surface seasonal oscillations and 3-D crustal deformation of the Tibetan Plateau derived from GPS and GRACE data. *Earth Planet. Sci. Lett.* **502**, 12–22 (2018).
65. Royden, L. H., Burchfiel, B. C. & van der Hilst, R. D. The geological evolution of the Tibetan Plateau. *Science* **321**, 1054–1058 (2008).
66. Holt, W. E. Correlated crust and mantle strain fields in Tibet. *Geology* **28**, 67–70 (2000).
67. Flesch, L. M., Haines, A. J. & Holt, W. E. Dynamics of the India-Eurasia collision zone. *J. Geophys. Res. Solid Earth* **106**, 16435–16460 (2001).
68. Wang, C.-Y., Flesch, L. M., Silver, P. G., Chang, L.-J. & Chan, W. W. Evidence for mechanically coupled lithosphere in central Asia and resulting implications. *Geology* **36**, 363–366 (2008).
69. Levin, V., Huang, G.-C.D. & Roecker, S. Crust-mantle coupling at the northern edge of the Tibetan plateau: evidence from focal mechanisms and observations of seismic anisotropy. *Tectonophysics* **584**, 221–229 (2013).
70. Wang, M. et al. Postseismic deformation of the 2008 Wenchuan earthquake illuminates lithospheric rheological structure and dynamics of Eastern Tibet. *J. Geophys. Res. Solid Earth* **126**, e2021JB022399 (2021).
71. Liu, Z. & Bird, P. Kinematic modelling of neotectonics in the Persia-Tibet-Burma orogen. *Geophys. J. Int.* **172**, 779–797 (2008).
72. Sternal, P. et al. On the influence of the asthenospheric flow on the tectonics and topography at a collision-subduction transition zones: comparison with the eastern Tibetan margin. *J. Geodyn.* **100**, 184–197 (2016).
73. Barbot, S., Hamiel, Y. & Fialko, Y. Space geodetic investigation of the coseismic and postseismic deformation due to the 2003 Mw 7.2 Altai earthquake: Implications for the local lithospheric rheology. *J. Geophys. Res.* **113**, B03403 (2008).
74. Hearn, E. H., McClusky, S., Ergintav, S. & Reilinger, R. E. Izmit earthquake postseismic deformation and dynamics of the North Anatolian Fault Zone. *J. Geophys. Res.* **114**, B08405 (2009).
75. Wang, L. et al. Afterslip and viscoelastic relaxation following the 1999 M 7.4 İzmit earthquake from GPS measurements. *Geophys. J. Int.* **178**, 1220–1237 (2009).
76. Rousset, B., Barbot, S., Avouac, J. P. & Hsu, Y.-J. Postseismic deformation following the 1999 Chi-Chi Earthquake, Taiwan: implication for lower-crust rheology. *J. Geophys. Res.* **117**, 16 (2012).
77. Ryder, I., Wang, H., Bie, L. & Rietbrock, A. Geodetic imaging of late postseismic lower crustal flow in Tibet. *Earth Planet. Sci. Lett.* **404**, 136–143 (2014).
78. Chanard, K., Fleitout, L., Calais, E., Barbot, S. & Avouac, J.-P. Constraints on transient viscoelastic rheology of the asthenosphere from seasonal deformation. *Geophys. Res. Lett.* **45**, 2328–2338 (2018).
79. Pollitz, F. F. Lithosphere and shallow asthenosphere rheology from observations of post-earthquake relaxation. *Phys. Earth Planet. Int.* **293**, 106271 (2019).
80. Argus, D. F., Peltier, W. R., Blewitt, G. & Kreemer, C. The viscosity of the top third of the lower mantle estimated using GPS, GRACE, and relative sea level measurements of glacial isostatic adjustment. *J. Geophys. Res.* **126**, e2020JB021537 (2021).
81. Diao, F., Wang, R., Xiong, X. & Liu, C. Overlapped postseismic deformation caused by afterslip and viscoelastic relaxation following the 2015 Mw 7.8 Gorkha (Nepal) earthquake. *J. Geophys. Res. Solid Earth* **126**, e2020JB020378 (2021).
82. Taylor, M. & Yin, A. Active structures of the Himalayan-Tibetan orogen and their relationships to earthquake distribution, contemporary strain field, and Cenozoic volcanism. *Geosphere* **5**, 199–214 (2009).
83. He, J. & Chery, J. Slip rates of the Altyn Tagh, Kunlun and Karakorum faults (Tibet) from 3D mechanical modeling. *Earth Planet. Sci. Lett.* **274**, 50–58 (2008).
84. Laske, G., Masters, G., Ma, Z. & Pasyanos, M. Update on CRUST1. 0–A 1-degree global model of Earth’s crust. In *Geophys. Res. Abstr.*, vol. 15, 2658 (EGU General Assembly Vienna, Austria, 2013).
85. Burrov, E. B. & Watts, A. B. The long-term strength of continental lithosphere: “jelly sandwich” or “crème brûlée”? *GSA Today* **16**, 4–10 (2006).
86. Bürgmann, R. & Dresen, G. Rheology of the lower crust and upper mantle: evidence from rock mechanics, geodesy, and field observations. *Ann. Rev. Earth Plan. Sci.* **36**, 531–567 (2008).
87. Wittlinger, G. P. et al. Tomographic evidence for localized lithospheric shear along the Altyn Tagh fault. *Science* **282**, 74–76 (1998).
88. Zhao, J. et al. The boundary between the Indian and Asian tectonic plates below Tibet. *Proc. Nat. Acad. Sci.* **107**, 11229–11233 (2010).
89. Allègre, C. J. et al. Structure and evolution of the Himalaya-Tibet orogenic belt. *Nature* **307**, 17–22 (1984).
90. Rao, W. & Sun, W. Moho interface changes beneath the Tibetan Plateau based on GRACE Data. *J. Geophys. Res. Solid Earth* **126**, e2020JB020605 (2021).
91. Wu, Y. et al. High-precision vertical movement and three-dimensional deformation pattern of the Tibetan Plateau. *J. Geophys. Res. Solid Earth* **127**, e2021JB023202 (2022).
92. Shapiro, N., Ritzwoller, M., Molnar, P. & Levin, V. Thinning and flow of Tibetan crust constrained by seismic anisotropy. *Science* **305**, 233–236 (2004).
93. Molnar, P. & Tapponnier, P. Active tectonics of Tibet. *J. Geophys. Res.* **83**, 5361–5375 (1978).
94. Tapponnier, P., Peltzer, G. & Armijo, R. On the mechanics of the collision between India and Asia. *Geol. Soc. London, Special Publications* **19**, 113–157 (1986).

95. Wang, S.-z, Sun, J.-x & Ning, J.-y Numerical simulation of ductile shear localization: Plastic-flow network and slip-line field. *Int. J. Numer. Anal. Methods Geomech.* **32**, 307–324 (2008).
96. Fu, Y. & Freymueller, J. T. Seasonal and long-term vertical deformation in the Nepal Himalaya constrained by GPS and GRACE measurements. *J. Geophys. Res. Solid Earth* **117** <https://agupubs.onlinelibrary.wiley.com/doi/abs/10.1029/2011JB008925> (2012).
97. Owens, T. J. & Zandt, G. Implications of crustal property variations for models of Tibetan plateau evolution. *Nature* **387**, 37–43 (1997).
98. Huang, J. & Zhao, D. High-resolution mantle tomography of China and surrounding regions. *J. Geophys. Res.* **111**, B09305 (2006).
99. Li, C., Van der Hilst, R. D., Meltzer, A. S. & Engdahl, E. R. Subduction of the Indian lithosphere beneath the Tibetan Plateau and Burma. *Earth Planet. Sci. Lett.* **274**, 157–168 (2008).
100. Wei, W., Xu, J., Zhao, D. & Shi, Y. East Asia mantle tomography: new insight into plate subduction and intraplate volcanism. *J. Asian Earth Sci.* **60**, 88–103 (2012).
101. Li, J. & Song, X. Tearing of Indian mantle lithosphere from high-resolution seismic images and its implications for lithosphere coupling in southern Tibet. *Proc. Natl Acad. Sci.* **115**, 8296–8300 (2018).
102. Fialko, Y. & Jin, Z. Simple shear origin of the cross-faults ruptured in the 2019 Ridgecrest earthquake sequence. *Nat. Geosci.* **14**, 513–518 (2021).
103. Li, C., van der Hilst, R. D., Engdahl, E. R. & Burdick, S. A new global model for P wave speed variations in Earth's mantle. *Geochem. Geophys. Geosyst.* **9**, Q05018 (2008).
104. Kufner, S.-K. et al. Seismic anisotropy beneath the Pamir and the Hindu Kush: evidence for contributions from crust, mantle lithosphere, and asthenosphere. *J. Geophys. Res. Solid Earth* **123**, 10,710–727,748 (2018).
105. Negredo, A. M., Replumaz, A., Villaseñor, A. & Guillot, S. Modeling the evolution of continental subduction processes in the Pamir–Hindu Kush region. *Earth Planet. Sci. Lett.* **259**, 212–225 (2007).
106. Liang, Y., Li, L., Liao, J. & Gao, R. Interaction of the Indian and Asian plates under the Pamir and Hindu-Kush regions: insights from 3-D shear wave velocity and anisotropic structures. *Geochem. Geophys. Geosyst.* **21**, e2020GC009041 (2020).
107. Kufner, S.-K. et al. The Hindu Kush slab break-off as revealed by deep structure and crustal deformation. *Nat. Commun.* **12**, 1685 (2021).
108. Schneider, F. et al. Seismic imaging of subducting continental lower crust beneath the Pamir. *Earth Planet. Sci. Lett.* **375**, 101–112 (2013).
109. Kufner, S.-K. et al. Deep India meets deep Asia: lithospheric indentation, delamination and break-off under Pamir and Hindu Kush (Central Asia). *Earth Planet. Sci. Lett.* **435**, 171–184 (2016).
110. Zhang, H. et al. Upper mantle heterogeneity and radial anisotropy beneath the Western Tibetan Plateau. *Tectonics* **40**, e2020TC006403 (2021).
111. Sobel, E. R. et al. Oceanic-style subduction controls late Cenozoic deformation of the Northern Pamir orogen. *Earth Planet. Sci. Lett.* **363**, 204–218 (2013).
112. Zhao, W. et al. Tibetan plate overriding the Asian plate in central and northern Tibet. *Nat. Geosci.* **4**, 870–873 (2011).
113. England, P. & McKenzie, D. A thin viscous sheet model for continental deformation. *Geophys. J. Int.* **70**, 295–321 (1982).
114. Royden, L. H. et al. Surface deformation and lower crustal flow in eastern Tibet. *Science* **276**, 788–790 (1997).
115. Willett, S. D. & Beaumont, C. Subduction of Asian lithospheric mantle beneath Tibet inferred from models of continental collision. *Nature* **369**, 642–645 (1994).
116. Yin, A. & Harrison, T. M. Geologic evolution of the Himalayan-Tibetan Orogen. *Annu. Rev. Earth Planet. Sci.* **28**, 211–280 (2000).
117. Spicer, R. A. et al. Why 'the uplift of the Tibetan Plateau' is a myth. *Natl Sci. Rev.* **8**, nwa091 (2021).
118. Liang, X. et al. 3D imaging of subducting and fragmenting Indian continental lithosphere beneath southern and central Tibet using body-wave finite-frequency tomography. *Earth Planet. Sci. Lett.* **443**, 162–175 (2016).
119. Pei, S., Liu, H., Bai, L., Liu, Y. & Sun, Q. High-resolution seismic tomography of the 2015 Mw7.8 Gorkha earthquake, Nepal: evidence for the crustal tearing of the Himalayan rift. *Geophys. Res. Lett.* **43**, 9045–9052 (2016).
120. Pan, Y. et al. GPS imaging of vertical bedrock displacements: quantification of two-dimensional vertical crustal deformation in China. *J. Geophys. Res. Solid Earth* **126**, e2020JB020951 (2021).
121. Currie, B. S. et al. Multiproxy paleoaltimetry of the late Oligocene-Pliocene Oiyug basin, southern Tibet. *Am. J. Sci.* **316**, 401–436 (2016).
122. Khan, M. A. et al. Miocene to Pleistocene floras and climate of the Eastern Himalayan Siwaliks, and new palaeoelevation estimates for the Namling–Oiyug Basin, Tibet. *Glob. Planet. Change* **113**, 1–10 (2014).
123. Saylor, J. E. et al. The late Miocene through present paleoelevation history of southwestern Tibet. *Am. J. Sci.* **309**, 1–42 (2009).
124. Graham, S. A. et al. Stable isotope records of Cenozoic climate and topography, Tibetan plateau and Tarim basin. *Am. J. Sci.* **305**, 101–118 (2005).
125. Yuan, D.-Y. et al. The growth of northeastern Tibet and its relevance to large-scale continental geodynamics: a review of recent studies. *Tectonics* **32**, 1358–1370 (2013).
126. Wang, C. et al. Outward-growth of the Tibetan Plateau during the Cenozoic: a review. *Tectonophysics* **621**, 1–43 (2014).
127. Thatcher, W. Microplate versus continuum descriptions of active tectonic deformation. *J. Geophys. Res. Solid Earth* **100**, 3885–3894 (1995).
128. Jolivet, R. et al. Shallow creep on the Haiyuan Fault (Gansu, China) revealed by SAR Interferometry. *J. Geophys. Res.* **117**, 18 (2012).
129. Meade, B. Algorithms for the calculation of exact displacements, strains, and stresses for triangular dislocation elements in a uniform elastic half space. *Comp. Geosc.* **33**, 1064–1075 (2007).
130. Barbot, S., Moore, J. D. & Lambert, V. Displacement and stress associated with distributed anelastic deformation in a half-space. *Bull. Seism. Soc. Am.* **107**, 821–855 (2017).
131. Barbot, S. Deformation of a half-space from anelastic strain confined in a tetrahedral volume. *Bull. Seism. Soc. Am.* **108**, 2687 (2018).
132. Anderson, E. *The Dynamics Faulting*. (Oliver and Boyd, London, 1951).
133. Allen, M. B., Vincent, S. J. & Wheeler, P. J. Late Cenozoic tectonics of the Kepingtage thrust zone: Interactions of the Tien Shan and Tarim Basin, northwest China. *Tectonics* **18**, 639–654 (1999).
134. Wang, L. & Barbot, S. Three-dimensional kinematics of the India-Eurasia collision. <https://doi.org/10.5281/zenodo.7771626> (2023).
135. Ekström, G., Nettles, M. & Dziewoński, A. M. The global CMT project 2004–2010: Centroid-moment tensors for 13,017 earthquakes. *Phys. Earth Planet. Inter.* **200–201**, 1–9 (2012).

## Acknowledgements

L.W. is supported by the National Natural Science Foundation of China under grant number NSFC-41674067, NSFC-U1839211 and NSFC-U2239204. S.B. is supported in part by the National Science Foundation under award number EAR-1848192. The constructive comments from three anonymous reviewers helped improve the manuscript. The authors thank Jinli Huang and Wei Wei for helping with the seismic velocity data.

## Author contributions

L.W. and S.B. designed the project, conducted the analysis, and wrote the manuscript.

## Competing interests

There are no competing interests. S.B. is an Editorial Board Member for Communications Earth & Environment, but was not involved in the editorial review of, nor the decision to publish this article.

## Additional information

**Supplementary information** The online version contains supplementary material available at <https://doi.org/10.1038/s43247-023-00815-4>.

**Correspondence** and requests for materials should be addressed to Lifeng Wang or Sylvain Barbot.

**Peer review information** *Communications Earth & Environment* thanks the anonymous reviewers for their contribution to the peer review of this work. Primary Handling Editor: Joe Aslin.

**Reprints and permission information** is available at <http://www.nature.com/reprints>

**Publisher's note** Springer Nature remains neutral with regard to jurisdictional claims in published maps and institutional affiliations.



**Open Access** This article is licensed under a Creative Commons Attribution 4.0 International License, which permits use, sharing, adaptation, distribution and reproduction in any medium or format, as long as you give appropriate credit to the original author(s) and the source, provide a link to the Creative Commons license, and indicate if changes were made. The images or other third party material in this article are included in the article's Creative Commons license, unless indicated otherwise in a credit line to the material. If material is not included in the article's Creative Commons license and your intended use is not permitted by statutory regulation or exceeds the permitted use, you will need to obtain permission directly from the copyright holder. To view a copy of this license, visit <http://creativecommons.org/licenses/by/4.0/>.

© The Author(s) 2023